DOI: 10.1002/((please add manuscript number))
Article type: Communication

$MoS_{0.5}Se_{1.5}$ Embedded in Two-dimensionally Porous Carbon Sheets Boost Lithium Storage Performance as An Anode Material

Tongfei Li,[#] Ao Wang,[#] Xin Li, Jingchun Wang, Jie Zhang, Gengtao Fu, Lin Xu, Dongmei Sun and Yawen Tang**

T. Li, X. Li, J. Wang, J. Zhang, Dr. G. Fu, Prof. L. Xu, Prof. D. Sun, Prof. Y. Tang
Jiangsu Key Laboratory of New Power Batteries, Jiangsu Collaborative Innovation Centre of Biomedical Functional Materials, School of Chemistry and Materials Science, Nanjing Normal University, Nanjing 210023, China
E-mail: gengtaofu@gmail.com (Gengtao Fu); tangyawen@njnu.edu.cn (Yawen Tang)

Dr. A. Wang
Institute of Chemical Industry of Forest Products, CAF, Key Lab of Biomass Energy and Material, Jiangsu Province, National Engineering Lab For Biomass Chemical Utilization, Key and Open Lab of Forest Chemical Engineering, SFA, No. 16, Suojin 5th Village, Nanjing 210042, China.

Dr. G. Fu
School of Chemical and Biomedical Engineering, Nanyang Technological University, Singapore 637459, Singapore
gengtaofu@gmail.com (Gengtao Fu)

Keywords: $MoS_{0.5}Se_{1.5}$; Porous carbon sheets; KCl-template; Anode; Li-ion batteries

In this work, we develop a promising anode material for Li-ion batteries consisting of $MoS_{0.5}Se_{1.5}$ particles (～15.3 nm) uniformly embedded in two-dimensionally (2D) porous carbon sheets (denoted as $MoS_{0.5}Se_{1.5}$/C sheets). The formation of $MoS_{0.5}Se_{1.5}$/C sheets depends on a facile and cost-effective potassium chloride (KCl)-assisted strategy. The micron-level KCl crystals are selected as the solid template because they are more easily precipitated than metal precursors and carbon source during recrystallization, which drives the simultaneous formation of carbon sheets and $MoS_{0.5}Se_{1.5}$ particles on KCl surface after pyrolysis; while makes a tighter integration between $MoS_{0.5}Se_{1.5}$ and carbon sheets. As an anode for Li-ion batteries, the $MoS_{0.5}Se_{1.5}$/C sheets show more excellent Li storage properties compared to that of S-free $MoSe_2$/C sheets, including excellent cyclic stability and high rate capacity. Specifically, 494.8 mA h g^{-1} at a current density of 100 mA g^{-1} still maintained for

$MoS_{0.5}Se_{1.5}$/C sheets after 200 cycles, which much higher than that of $MoSe_2$/C sheets (173.5 mA h g^{-1}). The significantly enhanced performance of $MoS_{0.5}Se_{1.5}$/C sheets can be attributed to the synergistic combination of $MoS_{0.5}Se_{1.5}$ phase and porous carbon sheets, which provides an effective conductive matrix and buffer spaces for Li-ion/electronic transfer and $MoS_{0.5}Se_{1.5}$ expansion, during the charge-discharge. The present method would open a new routine for the preparation of anode material, especially for the Mo-based materials in Li-ion batteries.

Lithium ion (Li-ion) batteries have been powering portable electronics since their emergence in the early 1990s,[1] however, their limited energy and power density impedes further extension of application to automobiles. To achieve the increase in energy and power density of Li-ion batteries, the development of effective electrode materials is essential.[2-5] Currently, the commercial anode materials of Li-ion batteries are dependent heavily on graphite carbon,[6-9] but the low theoretical capacity (372 mAh g^{-1}) and relatively poor rate capability cannot meet the increasing demands in Li-ion batteries.[10-13] Therefore, developing the alternative anode materials to meet the demands of future battery-units is an urgent task.

Emerging as a class of potential alternative, transition metal dichalcogenides (TMDs), MX_2 (M = Mo, W, Co, Sn; X = S, Se),[14-30] have been in the spotlight recently as anode materials because of their open 2D layered structure, and high theoretical specific capacity as well as remarkable electronic properties. Atoms within 2D layers are bound via strong covalent-bonds (X–M–X), while the bonding between layers and layers is through weak van der Waals force forming a sandwich-like structure,[31, 32] which favors the intercalation/deintercalation of Li-ions. Relative to widely studied MoS_2 (interlayer space: 0.615 nm), $MoSe_2$ possesses lager interlayer space of about ~0.646 nm and smaller band gap of ~1.5 eV,[33-35] thus the excellent Li-ion storage performance of $MoSe_2$ can be expected. As a semiconductor, the inherently inferior electrochemical conductivity of $MoSe_2$ still significantly impends the practical available in the case of large current charge/discharge. On the other hand, the intrinsic layer

structure of $MoSe_2$ generally inclines to restack in the cyclic course, resulting in rapidly fading of reversible capacity and unsatisfying cyclic stability. Therefore, the incorporation of more conductively compositions and building robust structure is desirable to enhanced electrochemical performance of $MoSe_2$-based materials in Li-ion batteries, yet still challenging.

Herein, we design an effective and general KCl-assisted strategy to synthesize S-doped $MoSe_2$ ($MoS_{0.5}Se_{1.5}$) that homogeneously embedded in 2D porous graphitic carbon sheets (denoted as $MoS_{0.5}Se_{1.5}$/C sheets) as a promising anode of Li-ion batteries. To the best of our knowledge, such KCl-assisted strategy has never been reported for the synthesis of 2D carbon sheets supported $MoS_{0.5}Se_{1.5}$ materials. We found that the incorporation of S could greatly improve electronic conductivity of $MoSe_2$ materials; while embedding $MoS_{0.5}Se_{1.5}$ particles within the 2D carbon sheets stabilizes the composite to give a superior long-term cycling stability. Compared with $MoSe_2$/C sheets, the $MoS_{0.5}Se_{1.5}$/C sheets can deliver the higher initial discharge and charge capacities of 1623.3 and 858.9 mAh g^{-1} at the current of 100 mA g^{-1} in a voltage of 0.1–3.0 V. At a current density of 100 mA g^{-1}, a reversible Li storage capacity of 494.8 mAh g^{-1} for up to 200 cycles can be obtained, much higher than that of $MoSe_2$/C sheets (173.5 mA h g^{-1}).

Figure 1a schematically shows the synthetic route of $MoS_{0.5}Se_{1.5}$/C sheets. The three steps were involved in the whole preparation process. In the first step, the reaction precursors were mixed together and grind evenly, then a certain amount of deionized water was added to dissolve the precursors and a part of KCl nanocrystals. The excessive KCl salts were selected as the template because that they easily recrystallize during the dried process making the precursors fully deposit around their surface; while the excessive KCl involved during the synthesis can effectively avoid the agglomeration of the resulting products. The second step involves the formation of $MoS_{0.5}Se_{1.5}$/C-coated KCl hybrid via thermal decomposition of metal salts and carbon source. Owing to the release of gases

during pyrolysis, a porous nanostructure can be effectively obtained. Finally, the obtained $MoS_{0.5}Se_{1.5}$/C-coated KCl hybrid was treated with deionized water/ethanol to remove the KCl template, resulting in the formation of porous $MoS_{0.5}Se_{1.5}$/C sheets. Crystal structure of $MoS_{0.5}Se_{1.5}$/C sheets was characterized with X-ray powder diffraction (XRD). As shown in Figure 1b, the product exhibits a typical hexagonal structure with high crystallinity after pyrolysis. The diffraction peaks at 13.9 º, 27.8 º, 31.7 º, 38.3 º, 42.3 º, 48.0 º, 53.8 º, 56.5 º, 57.3 º, 66.7 º and 73.6 º can be assigned to (002), (004), (100), (103), (006), (105), (106), (110), (008), (201) and (204) planes of hexagonal 2H-structural $MoS_{0.5}Se_{1.5}$ (JCPDS No. 36-1410), respectively. The distinctive diffraction peak appearing at around 26 º is corresponding to (002) peak of the graphited carbon. The atom ratio of Mo, S and Se is approximately 33.6%, 16.2% and 50.2% based on energy-dispersive X-ray (EDX) spectrum (Figure 1c), in agreement with the stoichiometric ratio. Weight-content of $MoS_{0.5}Se_{1.5}$ in $MoS_{0.5}Se_{1.5}$/C sheets was determined with thermogravimetric analysis (TGA, Figure 1d), during which $MoS_{0.5}Se_{1.5}$ was converted to MoO_3 and SeO_2 completely and carbon was oxidized to CO_2. Note that SeO_2 and CO_2 would be evaporated completely during the TG measurement. Based on the final content of oxides (MoO_3), the weight-content of $MoS_{0.5}Se_{1.5}$ was calculated to be about 57.60 %.

Morphology and structure of $MoS_{0.5}Se_{1.5}$/C sheets were first investigated with scanning electron microscopy (SEM) technology (**Figure 2**a-2c). As observed, the obtained product exhibits a typical 2D porous sheet-like structures (Figure 2a), in which particles are homogeneously embedded (Figure 2b). The thickness of carbon sheets was estimated to be approximately 15.4 nm taken from a cross-section of a single $MoS_{0.5}Se_{1.5}$/C sheet (Figure 2c). Transmission electron microscopy (TEM) images (Figure 2d-2e) further confirmed that $MoS_{0.5}Se_{1.5}$ particles are homogeneously dispersed on carbon nanosheets, in according with SEM results. The histogram of $MoS_{0.5}Se_{1.5}$ particle diameters was recorded from a sampling size of 100 particles in random regions (Figure 2f), which manifests a relatively narrow

particle-size distribution with an average size of 15.3 nm. The interplanar spacing of the adjacent fringes was measured to be 0.311 nm based on high-resolution TEM (HRTEM, Figure S1), which matches well with the (004) facet of $MoS_{0.5}Se_{1.5}$ (JCPDS No. 36-1410). Figure 2g shows the EDX elemental mappings of $MoS_{0.5}Se_{1.5}$/C sheets, which clearly reveals the uniform distributions of C, S, Mo and Se elements throughout the $MoS_{0.5}Se_{1.5}$/C sheets. For a comparison, the S-free $MoSe_2$/C sheets were also synthesized through similar steps to $MoS_{0.5}Se_{1.5}$/C sheets, except for without addition of the C_2H_5NS. The detail characterizations of $MoSe_2$/C sheets were presented in Figure S2-S3. As observed, the $MoSe_2$/C shows the same structure as the $MoS_{0.5}Se_{1.5}$/C sheets, demonstrating that KCl functions as a template to effective direct the formation of 2D sheet-like structure.

The chemical state and surface composition of $MoS_{0.5}Se_{1.5}$/C sheets were evaluated with X-ray photoelectron spectroscopy (XPS) analysis. The peaks related to Mo, Se, S and C elements are all presented in full-XPS spectrum (Figure S4). **Figure 3**a shows the high-resolution Mo 3d XPS spectrum, in which the peaks centered at 228.5 eV and 231.8 eV are best fitted using Gaussian fitting method, corresponding to the typical Mo^{5+} $3d_{5/2}$ and Mo^{5+} $3d_{3/2}$ spin-orbits. The existence of S^{2-} species was also confirmed by the high-resolution S 2p XPS spectrum (Figure 3b). Two binding energies at 161.8 and 163.5 eV should be attributed to S^{2-} $2p_{3/2}$ and S^{2-} $2p_{1/2}$, respectively. The Se element within $MoS_{0.5}Se_{1.5}$/C sheets was mainly present in the form of zero-valent state (Se^0 $3d_{5/2}$: 54.5 eV; Se^0 $3d_{3/2}$: 55.4 eV), as depicted in Figure 3c. Additionally, the high-resolution C 1s spectrum could be deconvoluted into two peaks: carbon in C-C at 284.6 eV and carbon in C-O at 285.1 eV. Taking together, XPS results further demonstrats the successful synthesis of $MoS_{0.5}Se_{1.5}$/C sheets. The XPS spectra of $MoSe_2$/C sheets were presented in detail in Figure S5, depicting $MoSe_2$/C sheets were fabricated successfully.

To confirm the porosity of both $MoS_{0.5}Se_{1.5}$/C and $MoSe_2$/C sheets, N_2 adsorption-desorption measurements were carried out (**Figure 4**a). Both samples show the type-IV

isotherm curves with a distinctive hysteresis loop, hinting the existence of the micro-/mesoporous structures. The porosity of both samples was also reflected by the pore-size distributions (Figure 4b). According to Barrett–Joyner–Halenda (BJH) analysis, the pore-sizes of both sample are all centered at approximately 1.27 nm. The Brunauer–Emmett–Teller (BET) surface areas of $MoS_{0.5}Se_{1.5}$/C and $MoSe_2$/C sheets are up to of 1045.99 and 817.71 $m^2 g^{-1}$, respectively. It is worth mentioning that BET surface area of the obtained $MoS_{0.5}Se_{1.5}$/C sheets is larger than a mass of 2D carbon-based materials reported before (Table S1). Therefore, we rationally conclude that TMDs/C sheets with the porous structure and large surface area could be fabricated by KCl-assisted pyrolysis method. The release of gas during the thermal pyrolysis is mainly responsible for the formation of porous structure. Larger BET surface area and abundant porosity can provide more Li-ion diffusion channels in both carbon sheets and host materials, which favors the charge and electron transfer during the charge and discharge as well as alleviate the strain stress.[36-38] Figure 4c displays Raman spectra of both $MoS_{0.5}Se_{1.5}$/C and $MoSe_2$/C. For $MoS_{0.5}Se_{1.5}$/C sheets, the three characteristic peaks at about 269 cm^{-1}, 370 cm^{-1} and 397 cm^{-1} were observed clearly, which are assigned to E_{2g} (Mo-Se), E_{2g} (Mo-S) and A_{1g} (Mo-S) vibrational mode, respectively.[39-41] This result further demonstrates the successful formation of $MoS_{0.5}Se_{1.5}$ phase. For $MoSe_2$/C sheets, the Raman spectrum also exhibits the representative A_{1g} (Mo-Se) vibrational mode of $MoSe_2$ at about 249 cm^{-1}. The degree of graphitization of carbon sheets in both samples were also investigated by the peak intensity ratio of D band to G band (I_D/I_G). The smaller value of I_D/I_G, the higher degree of graphitization.[42, 43] The I_D/I_G ratio for $MoS_{0.5}Se_{1.5}$/C and $MoSe_2$/C sheets was calculated to be about 0.95 and 0.97, respectively, higher than that of reported activated-carbon (1.10).[42, 44] The result confirms the high graphitization degrees of both $MoS_{0.5}Se_{1.5}$/C and $MoSe_2$/C samples, which is beneficial to the improvement of their electrical conductivity, as verified by the four-point probe method. The electrical conductivity of $MoS_{0.5}Se_{1.5}$/C and $MoSe_2$/C sheets was measured to be 15.6×10^3 S m^{-1} and 6.61×10^3 S m^{-1}, respectively (Figure

4d). Note that the electrical conductivity of $MoS_{0.5}Se_{1.5}$/C is remarkably higher than that of $MoSe_2$, indicating that the doped of S efficient enhances the electrical conductively of $MoSe_2$, in accordance with the works reported before.[45, 46]

The electrochemical performance of $MoS_{0.5}Se_{1.5}$/C sheets was first evaluated by cyclic voltammograms (CVs) technique at a scan rate of 0.1 mV s^{-1} between 0.001 and 3.0 V *versus* Li/Li^+. As observed in **Figure 5**a, there are four obvious cathodic peaks in the first cathodic sweep. The cathodic peaks at 1.67 V, 1.56 V and 1.01 V can be attributed to the reductive decomposition of electrolyte or the formation of solid/electrolyte interphase.[45, 46] The fourth cathodic peak at around 0.51 V originates from the phase transition from 2H-$MoS_{0.5}Se_{1.5}$ to 1T-Lix$MoS_{0.5}Se_{1.5}$ due to the intercalation of Li-ions into the crystalline structure of $MoS_{0.5}Se_{1.5}$, which illustrated it's an irreversible process because that the reduction peak was not arise in the second CV scan process.[45, 47] In the reverse anodic scan, three oxidation peaks at 1.17 V, 1.78 V and 1.84 V were separately associated with the stepwise oxidation from Mo to Mo^{4+} and further to Mo^{6+} according to the works reported before;[48, 49] while another peak at 2.21 V corresponding to Li deintercalation from the sulfoselenides.[46] It is clear that the anodic peaks almost overlap during the following two positive scans, suggesting a highly reversible and stable deintercalation Li process of $MoS_{0.5}Se_{1.5}$/C sheets. Figure 5b shows the initial three galvanostatic discharge/charge curves of $MoS_{0.5}Se_{1.5}$/C sheets at the current density of 0.05 A g^{-1} within a potential range of 0.001-3.0 V *versus* Li/Li^+. The $MoS_{0.5}Se_{1.5}$/C sheets electrode delivers high first-cycle discharge and charge capacities of 1623.3 and 795.9 mA h g^{-1}, respectively, corresponding to a Coulombic efficiency of 49.0 %. The initial loss is mainly caused by the decomposition of the electrolyte,[50] or some irreversible processes such as the formation of a solid-electrolyte interface layer during the first cycle.[51] The discharge and charge capacities in the second cycle are 858.9 and 710.5 mA h g^{-1}, respectively, and give rise to a much higher Coulombic efficient of 82.7 %. The value further settled in around 82.3 % in

the third cycle, indicating the highly capacity reversibility of $MoS_{0.5}Se_{1.5}$/C sheets. Similar electrochemical performance of $MoSe_2$/C sheets in cyclic voltammogram and galvanostatic charge and discharge were exhibited in Figure S6.

The cycling behavior of both $MoS_{0.5}Se_{1.5}$/C and $MoSe_2$/C electrodes at a current density of 100 mA g^{-1} was plotted in Figure 5c. Both $MoS_{0.5}Se_{1.5}$/C and $MoSe_2$/C electrodes exhibit the different degrees of capacity fading. It is mainly caused by numerous irreversible chemical and/or electrochemical reactions occur in the electrodes, such as the decomposition of the electrolyte and dissolution of the electrode materials. For $MoS_{0.5}Se_{1.5}$/C electrode, the reversible discharge capacity could be maintained at 494.8 mA h g^{-1} after 200 cycles and the Coulombic efficient close to 100%. In contrast, $MoSe_2$/C electrode displays lower initial capacity and only a reversible capacity of 173.5 mA h g^{-1} is retained after 200 cycles. Obviously, the sample of $MoS_{0.5}Se_{1.5}$/C exhibits 2.9-fold as high as that of $MoSe_2$/C sample in the capacity retention value. The improved capacity of $MoS_{0.5}Se_{1.5}$/C may stem from the incorporation of S greatly improved electronic conductivity of $MoSe_2$ materials. The rate capability of $MoS_{0.5}Se_{1.5}$/C sheets and $MoSe_2$/C sheets anode was also evaluated at various current densities from 0.1 to 1.0 A g^{-1} (Figure 5d). The charge capacities of $MoS_{0.5}Se_{1.5}$/C are about 685.9, 529.7, 404.9 and 322.6 mA h g^{-1} at current densities of 0.1, 0.2, 0.5 and 1.0 A g^{-1}, respectively. When the current density goes back to 0.1 A g^{-1}, a stable capacity of 509.4 A g^{-1} can still be observed. This suggests that $MoS_{0.5}Se_{1.5}$/C anode is tolerant of high-rate operation, which obviously suppresses that of $MoSe_2$/C anode. The corresponding charge capacities decreased from 270.7, 207.4, 140.8 and 105.4 mA h g^{-1} at current densities ranging from 0.1 to 1.0 A g^{-1}. The capacity difference of $MoSe_2$/C sample was observed between Figure 5c and 5d, which may originate from the deviation mass of the electrode materials. The Li-ion batteries performance of $MoS_{0.5}Se_{1.5}$/C anode can be comparable or even superior than some recently reported Mo-based materials (Table S2).

After 200 cycles test at a current density of 100 mA g^{-1}, the structural change of $MoS_{0.5}Se_{1.5}$/C sheets was investigated with TEM technology. As indicated in Figure S7, the integrity of $MoS_{0.5}Se_{1.5}$ has been maintained well on carbon sheets, demonstrating excellent structure stability of $MoS_{0.5}Se_{1.5}$/C sheets. Based on the above results, the superior performance of $MoS_{0.5}Se_{1.5}$/C sheets can be mainly attributed to the follow reasons: (i) The incorporation of S greatly improved electronic conductivity of $MoSe_2$ materials, thus giving favorable ion/electron transport and diffusion; (ii) Embedding the $MoS_{0.5}Se_{1.5}$ particles within the 2D carbon sheets stabilizes the composite as the robust and flexible buffer matrix to relieve the volume expansion of active materials during the repeated Li-ion insertion/extraction processes, thereby generating a superior long-term cyclic stability; (iii) Abundant porosity and larger BET surface area is an effective approach to furnish numerous accessible active sites for penetration of the electrolyte into the host active materials, as well as facilitating charge-transfer reaction in electrode/electrolyte interface.

In summary, a promising anode material was developed for Li-ion batteries consisting of $MoS_{0.5}Se_{1.5}$ particles embedded in porous carbon sheets via a scalable and effective pyrolysis-based route with KCl crystals as a template. The electronic conductivity of $MoS_{0.5}Se_{1.5}$ (15.6×10^3 S m^{-1}) is greatly improved after S is introduced into $MoSe_2$ (6.61×10^3 S m^{-1}), which provides fast transport of both ions and electrons within the electrode. Meanwhile, the volume expansion and aggregation of $MoS_{0.5}Se_{1.5}$ can be avoided during lithiation/delithiation process benefiting from the intimate contact between $MoS_{0.5}Se_{1.5}$ and carbon sheets. Benefiting from fascinating structure and composition, the $MoS_{0.5}Se_{1.5}$/C sheets manifest outstanding lithium storage performance including high initial specific capacities of 858.9 mAh g^{-1} higher than $MoSe_2$/C sheets (783.1 mAh g^{-1}) at a current density of 100 mA g^{-1}; excellent rate capability and superior cycling stability at 494.8 mAh g^{-1} for 200 cycles. The satisfactory electrochemical performance can be

attributed to its superior conductivity, robust nanostructure and relative large surface area, making it a promising candidate as anode materials for Li-ion batteries.

Experimental Section

Reagents and chemicals

Ammonium molybdate tetrahydrate ($(NH_4)_6Mo_7O_{24}\cdot 4H_2O$), fructose ($C_6H_{12}O_6$), potassium chloride (KCl), sodium selenite (Na_2SeO_3), thioacetamide (C_2H_5NS) and ethanol were purchased from Sinopharm Chemical Reagent Co., Ltd. (Shanghai, China). All reagents and chemicals were used without further purification.

Synthesis of $MoS_{0.5}Se_{1.5}$/C sheets

Typically, 1.60 g fructose, 0.18 g $(NH_4)_6Mo_7O_{24}\cdot 4H_2O$, 6.0 g KCl, 0.35 g Na_2SeO_3 and 0.15 g C_2H_5NS were first mixed and manual ground in agate mortar for about 1.0 h. Then, 10 mL deionized water was added to the above mixture with stirring for 30 min. The resulting mixture was subsequently dried for 10 h in the oven at 40 ^oC for recrystallization of metal and carbon precursors on the surface of KCl nanocrystals. Finally, the mixture was calcined in a tube furnace at 750 ^oC under a flow of 5% H_2 in an Ar atmosphere for 6 h (ramp rate: 5 ^oC min^{-1}). After cooling to room temperature, the obtained black puffy powder was treated with deionized water and ethanol several times to remove KCl template, and dried at 60 ^oC to receive the final $MoS_{0.5}Se_{1.5}$/C sheets. For comparison, S-free $MoSe_2$/C sheets were also synthesized in a similar process, except for the without addition of the C_2H_5NS.

Characterization

The morphology, composition, and structure of the products were characterized by X-ray powder diffraction (XRD, Rigaku D/max 2500/PC), Scanning electron microscopy (SEM) images were obtained on a JSM-2010 microscope at an accelerating voltage of 20 kV and high-resolution transmission electron microscopy (HRTEM, JEOL JEM-2010F, 200 kV) coupled with an energy-dispersive X-ray spectrometer (EDX, Thermo Fisher Scientific).

Thermal analysis was carried out on a Perkin Elmer thermogravimetric analyzer under O_2 atmosphere over the temperature range of room temperature to 800 ^oC with a ramp rate of 10 ^oC/min. X-ray photoelectron spectroscopy (XPS) measurements were carried out on a Thermo VG Scientific ESCALAB 250 spectrometer. The Raman spectra were recorded on a Raman spectrometer (Lab RAM HR800, λ = 514 nm). Nitrogen adsorption and desorption measurement was performed at 77 K using a Micromeritics ASAP 2050 analyzer, and the surface area, pore volume, and pore diameter of the product were calculated using Brunauer–Emmett–Teller (BET) and Barrett–Joyner–Halenda (BJH) methods, respectively. The electrical conductivity was measured by 4-probe conductivity measurements on ST-2722 semiconductor resistivity of the powder tester (Suzhou Jingge Electronic Co., Ltd., PR China) under a pressure of 10 MPa.

Electrochemical Measurements

Lithium storage performance was carried out by 2025-type coin cells, which were assembled in an Ar-filled glove box (IL-2GB, Innovative Technology). The electrodes were made as follows: 70 wt % active material ($MoS_{0.5}Se_{1.5}$/C sheets), 20 wt % conductive material (Super P carbon black), and 10 wt % binder (polyvinyldifluoride, PVDF) were mixed in N-methyl-2-pyrrolidene (NMP), and then the anodic slurry was coated on copper foam current collectors and dried under vacuum at 120 ^oC for 12 h. The counter electrode was lithium foil, and the electrolyte solution was 1 M $LiPF_6$ in ethylene carbonate (EC) and dimethyl carbonate (DMC) (1:1 v: v). Cycling tests were carried out on a LANHE CT2001A battery tester (Wuhan LAND Electronics Co., Ltd.) in the potential range of 0.001-3.0 V.

Supporting Information

Supporting Information is available from the Wiley Online Library or from the author.

Acknowledgements

T. Li and A. Wang contributed equally to this work. This work is financially supported by National Natural Science Foundation of China (21503111, 21576139 and 21376122), Natural Science Foundation of Jiangsu Province (BK20171473), Natural Science Foundation of Jiangsu Higher Education Institutions of China (16KJB150020) and Key Laboratory of Renewable Energy, Chinese Academy of Sciences (Y607k51001). The authors also thank National and Local Joint Engineering Research Center of Biomedical Functional Materials and a project sponsored by the Priority Academic Program Development of Jiangsu Higher Education Institutions.

Received: ((will be filled in by the editorial staff))
Revised: ((will be filled in by the editorial staff))
Published online: ((will be filled in by the editorial staff))

[1] Z. Yang, J. Zhang, M. C. W. Kintner-Meyer, X. Lu, D. Choi, J. P. Lemmon and J. Liu, *Chem. Rev.* **2011**, *111*, 3577.

[2] H. K. Bruce Dunn, Jean-Marie Tarascon, *Science* **2011**, *334*, 928.

[3] J. Wan, J. Zhang, J. Yu and J. Zhang, *ACS Appl. Mater. Interfaces* **2017**, *9*, 24591.

[4] Y. Cheng, J. Huang, H. Qi, L. Cao, J. Yang, Q. Xi, X. Luo, K. Yanagisawa and J. Li, *Small* **2017**, *13*, 1700656.

[5] L. Zhang, K. Zhao, R. Yu, M. Yan, W. Xu, Y. Dong, W. Ren, X. Xu, C. Tang and L. Mai, *Small* **2017**, *13*, 1603973.

[6] J. Z. Han Hu, Buyuan Guan, and Xiong Wen(David) Lou, *Angew. Chem., Int. Ed.* **2016**, *55*, 9514.

[7] S. Wang, B. Y. Guan, L. Yu and X. W. D. Lou, *Adv. Mater.* **2017**, *29*, 1702724.

[8] Y. Chen, Y. Hu, Z. Shen, R. Chen, X. He, X. Zhang, Y. Li and K. Wu, *J. Power Sources* **2017**, *342*, 467.

[9] C. Deng, M. L. Lau, H. M. Barkholtz, H. Xu, R. Parrish, M. O. Xu, T. Xu, Y. Liu, H. Wang, J. G. Connell, K. A. Smith and H. Xiong, *Nanoscale* **2017**, *9*, 10757.

[10] X.-M. Zheng, P.-Y. Zhang, L.-K. Wang, S. Tao, Y.-X. Wang, L. Huang, J.-T. Li and S.-G. Sun, *Electrochim. Acta* **2017**, *247*, 314.

[11] C. H. Jian Qin, Naiqin Zhao, ZhiyuanWang, Chunsheng Shi, En-Zuo Liu, and Jiajun Li, *ACS Nano* **2014**, *8*, 1728.

[12] L. Yang, X. Li, Y. Ouyang, Q. Gao, L. Ouyang, R. Hu, J. Liu and M. Zhu, *ACS Appl. Mater. Interfaces* **2016**, *8*, 19987.

[13] S. Zhu, J. Li, X. Deng, C. He, E. Liu, F. He, C. Shi and N. Zhao, *Adv. Funct. Mater.* **2017**, *27*, 1605017.

[14] Y. Zhang, T. He, G. Liu, L. Zu and J. Yang, *Nanoscale* **2017**, *9*, 10059.

[15] Y. Jing, E. O. Ortiz-Quiles, C. R. Cabrera, Z. Chen and Z. Zhou, *Electrochim. Acta* **2014**, *147*, 392.

[16] Y. Wang, D. Kong, W. Shi, B. Liu, G. J. Sim, Q. Ge and H. Y. Yang, *Adv. Energy Mater.* **2016**, *6*, 1601057.

[17] Y. Liu, W. Wang, Y. Wang and X. Peng, *Nano Energy* **2014**, *7*, 25.

[18] T. Xiang, S. Tao, W. Xu, Q. Fang, C. Wu, D. Liu, Y. Zhou, A. Khalil, Z. Muhammad, W. Chu, Z. Wang, H. Xiang, Q. Liu and L. Song, *ACS Nano* **2017**, *11*, 6483.

[19] Y. Liu, M. Zhu and D. Chen, *J. Mater. Chem. A* **2015**, *3*, 11857.

[20] W. Yang, J. Wang, C. Si, Z. Peng and Z. Zhang, *Nano Res.* **2017**, *10*, 2584.

[21] Q. Wang, R. Zou, W. Xia, J. Ma, B. Qiu, A. Mahmood, R. Zhao, Y. Yang, D. Xia and Q. Xu, *Small* **2015**, *11*, 2511.

[22] W. Qiu, J. Jiao, J. Xia, H. Zhong and L. Chen, *Chem. Eur. J.* **2015**, *21*, 4359.

[23] Z. Xiang Huang, B. Liu, D. Kong, Y. Wang and H. Ying Yang, *Energy Storage Mater.* **2018**, *10*, 92.

[24] C. Ling, Y. Huang, H. Liu, S. Wang, Z. Fang and L. Ning, *J. Phys. Chem. C* **2014**, *118*, 28291.

[25] B. Luo, Y. Fang, B. Wang, J. Zhou, H. Song and L. Zhi, *Energy Environ. Sci.* **2012**, *5*, 5226.

[26] G. Wang, J. Peng, L. Zhang, J. Zhang, B. Dai, M. Zhu, L. Xia and F. Yu, *J. Mater. Chem. A* **2015**, *3*, 3659.

[27] J. Xu, J. Zhang, W. Zhang and C.-S. Lee, *Adv. Energy Mater.* **2017**, DOI: 10.1002/aenm.201700571.

[28] G. Xu, L. Yang, X. Wei, J. Ding, J. Zhong and P. K. Chu, *Adv. Funct. Mater.* **2016**, *26*, 3349.

[29] G. D. Park, J. H. Kim, S.-K. Park and Y. C. Kang, *ACS Appl. Mater. Interfaces* **2017**, *9*, 10673.

[30] W. Tang, D. Xie, T. Shen, X. Wang, D. Wang, X. Zhang, X. Xia, J. Wu and J. Tu, *Chem. Eur. J.* **2017**, *23*, 12924.

[31] Y. Liu, M. Zhu and D. Chen, *J. Mater. Chem. A* **2015**, *3*, 11857.

[32] M. Pumera, Z. Sofer and A. Ambrosi, *J. Mater. Chem. A* **2014**, *2*, 8981.

[33] Z. Zhang, Y. Fu, X. Yang, Y. Qu and Z. Zhang, *ChemNanoMat* **2015**, *1*, 409.

[34] C. Zheng, C. Chen, L. Chen and M. Wei, *J. Mater. Chem. A* **2017**, *5*, 19632.

[35] X. Zhao, J. Sui, F. Li, H. Fang, H. Wang, J. Li, W. Cai and G. Cao, *Nanoscale* **2016**, *8*, 17902.

[36] Y. Zhang, B. Tao, W. Xing, L. Zhang, Q. Xue and Z. Yan, *Nanoscale* **2016**, *8*, 7889.

[37] J. Yang, X. Zhou, D. Wu, X. Zhao and Z. Zhou, *Adv. Mater.* **2016**, *29*, 1604108.

[38] R. Dai, W. Sun, L. P. Lv, M. Wu, H. Liu, G. Wang and Y. Wang, *Small* **2017**, *13*, 1700521.

[39] P. Zhang, F. Qin, L. Zou, M. Wang, K. Zhang, Y. Lai and J. Li, *Nanoscale* **2017**, *9*, 12189.

[40] X. Zhang, R. Zhao, Q. Wu, W. Li, C. Shen, L. Ni, H. Yan, G. Diao and M. Chen, *ACS Nano* **2017**, *11*, 8429.

[41] F. Niu, J. Yang, N. Wang, D. Zhang, W. Fan, J. Yang and Y. Qian, *Adv. Funct. Mater.* **2017**, *27*, 1700522.

[42] G. Fu, Y. Chen, Z. Cui, Y. Li, W. Zhou, S. Xin, Y. Tang and J. B. Goodenough, *Nano Lett.* **2016**, *16*, 6516.

[43] G. Fu, Z. Cui, Y. Chen, Y. Li, Y. Tang and J. B. Goodenough, *Adv. Energy Mater.* **2017**, *7*, 1601172.

[44] G. Fu, Z. Liu, J. Zhang, J. Wu, L. Xu, D. Sun, J. Zhang, Y. Tang and P. Chen, *Nano Res.* **2016**, *9*, 2110.

[45] J. Zhang, W. Kang, M. Jiang, Y. You, Y. Cao, T. W. Ng, D. Y. Yu, C. S. Lee and J. Xu, *Nanoscale* **2017**, *9*, 1484.

[46] Z. T. Shi, W. Kang, J. Xu, L. L. Sun, C. Wu, L. Wang, Y. Q. Yu, D. Y. Yu, W. Zhang and C. S. Lee, *Small* **2015**, *11*, 5667.

[47] Y. N. Ko, S. H. Choi, S. B. Park and Y. C. Kang, *Nanoscale* **2014**, *6*, 10511.

[48] S. H. Choi and Y. C. Kang, *Nanoscale* **2016**, *8*, 4209.

[49] F. Wang, S. Song, J. Li, J. Pan, X. Wang and H. Zhang, *Nanoscale* **2017**, *9*, 6346.

[50] Y. Pan, J. Zhang and H. Lu, *Chem. Eur. J.* **2017**, *23*, 9937.

[51] N. Mahmood, J. Zhu, S. Rehman, Q. Li and Y. Hou, *Nano Energy* **2015**, *15*, 755.

Figures and captions

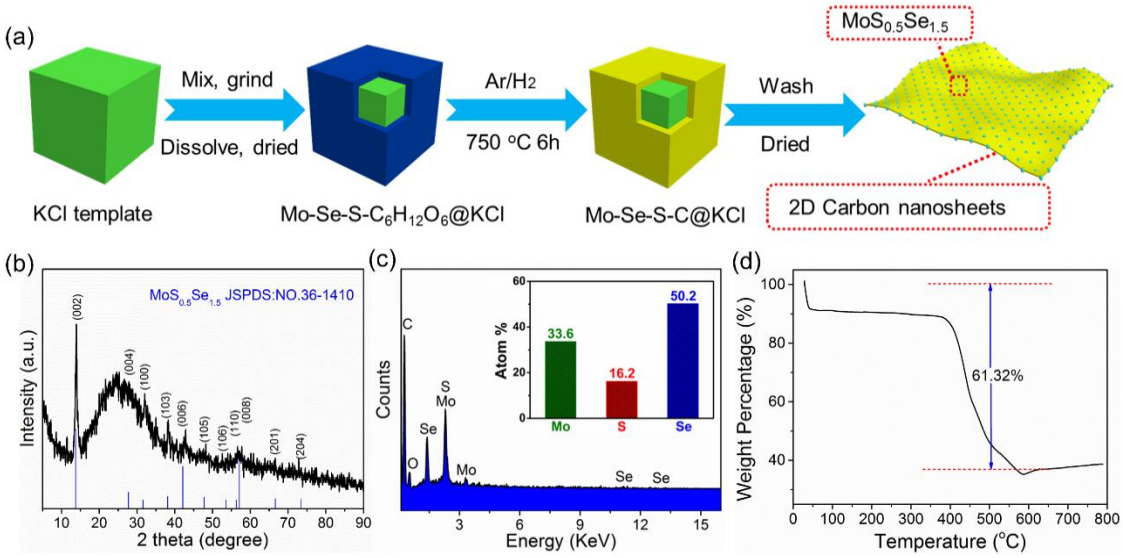

Figure 1. (a) Schematic showing the synthetic route of $MoS_{0.5}Se_{1.5}$/C sheets; (b) XRD pattern, (c) EDX spectrum and (d) TGA curve of $MoS_{0.5}Se_{1.5}$/C sheets.

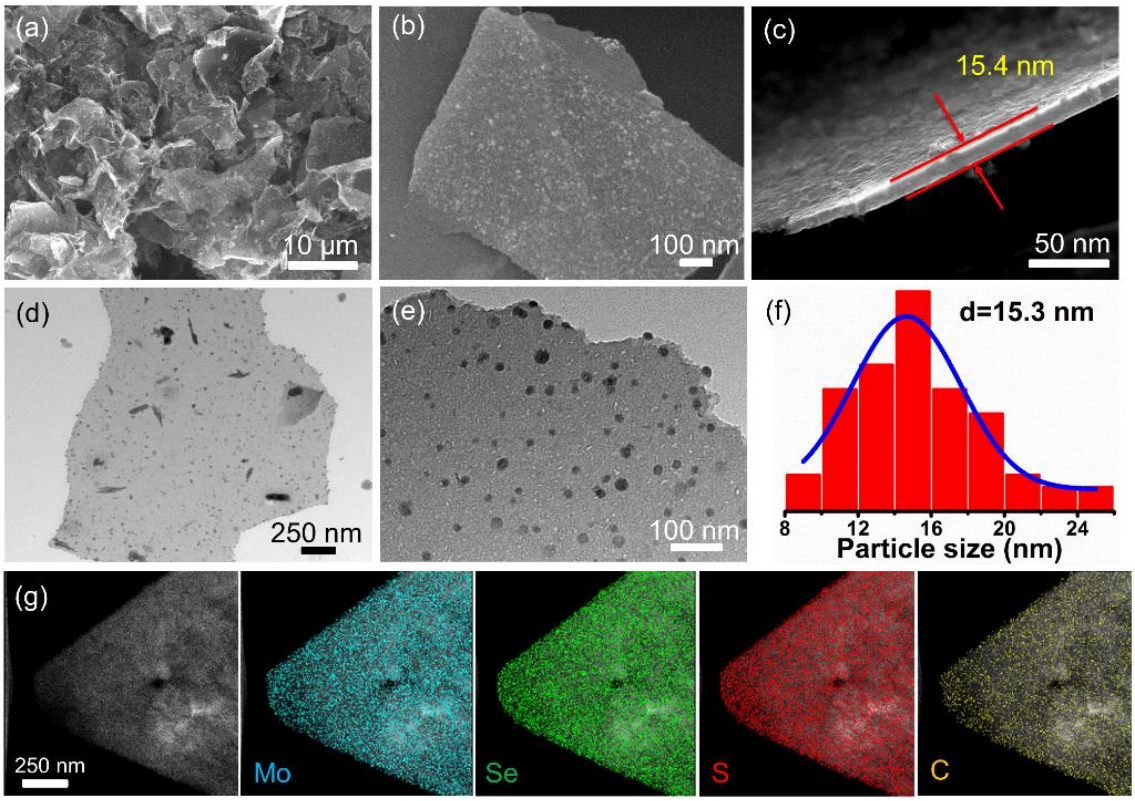

Figure 2. (a-c) SEM images, (d-e) TEM images, (f) particle size distribution and (g) STEM image and corresponding EDX elemental mappings of $MoS_{0.5}Se_{1.5}$/C sheets.

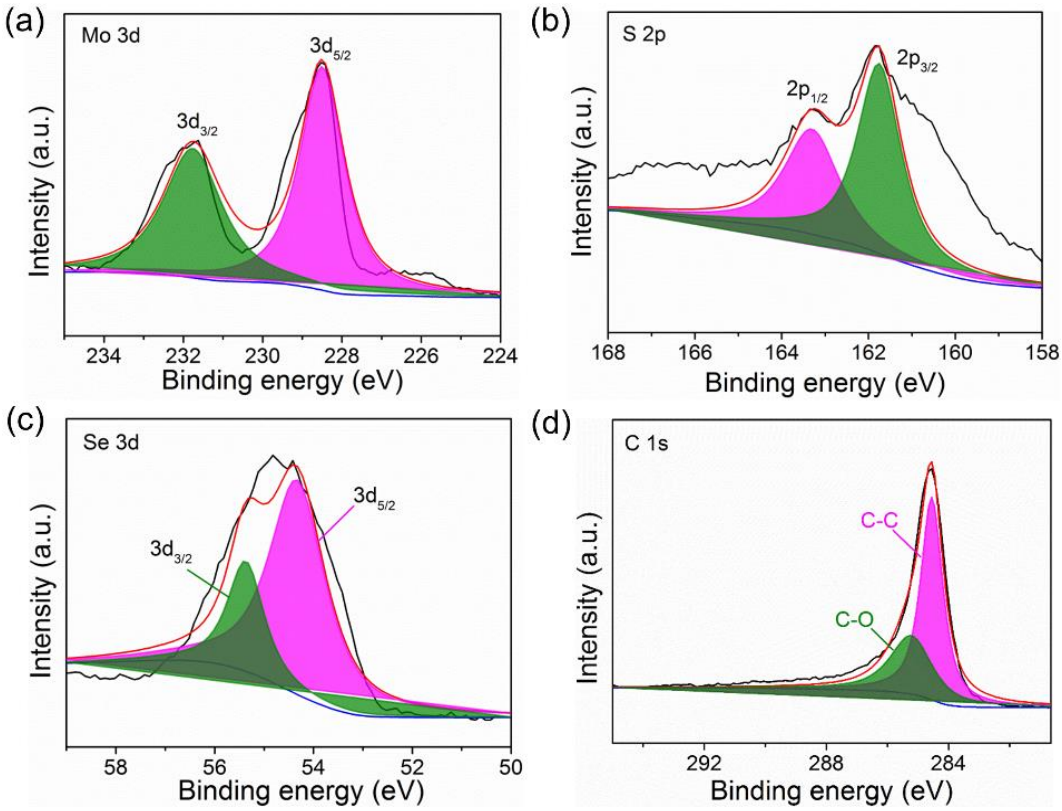

Figure 3. High-resolution XPS spectra of $MoS_{0.5}Se_{1.5}$/C sheets: (a) Mo 3d, (b) S 2p, (c) Se 3d, and (d) C 1s.

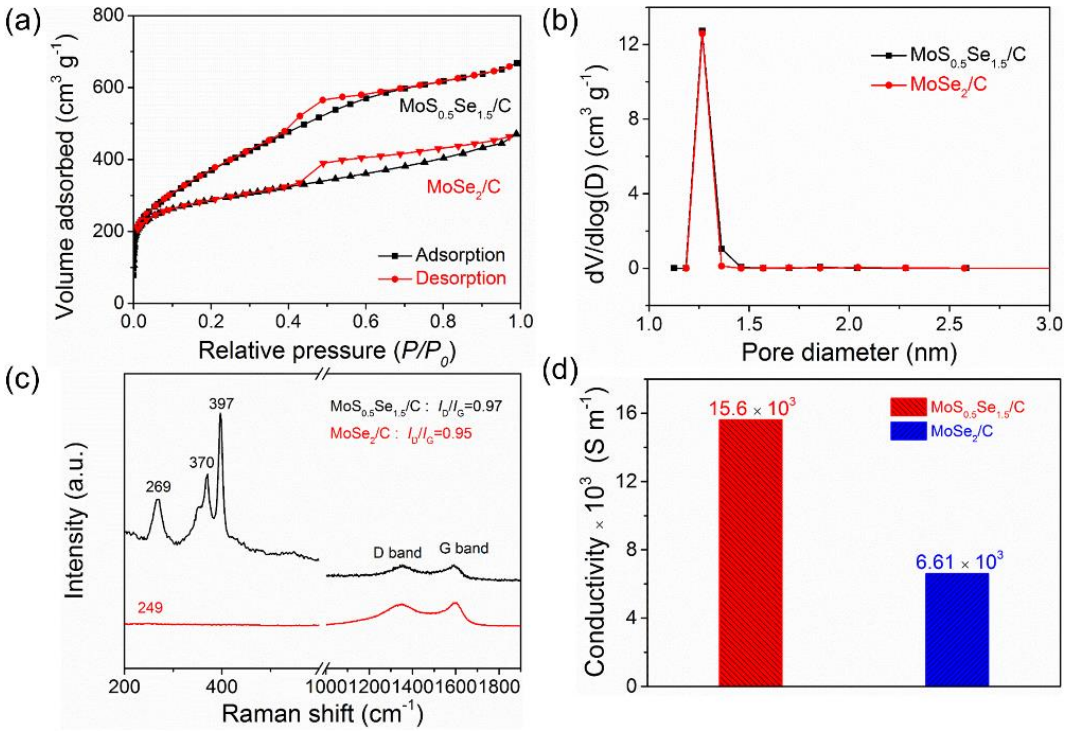

Figure 4. (a) N_2 adsorption-desorption isotherms and (b) the corresponding pore-size distribution curves of $MoS_{0.5}Se_{1.5}$/C and $MoSe_2$/C sheets; (c) Raman spectra and (d) electrical conductivities of $MoS_{0.5}Se_{1.5}$/C and $MoSe_2$/C sheets.

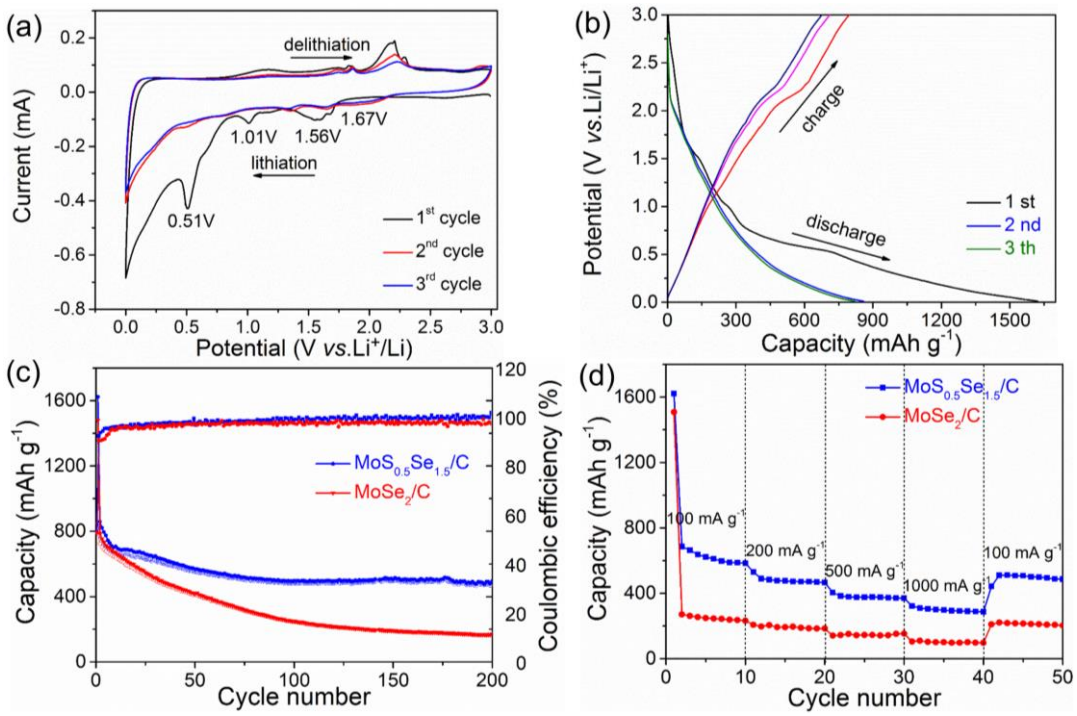

Figure 5. The electrochemical performance of $MoS_{0.5}Se_{1.5}$/C sheets and $MoSe_2$/C sheets: (a) Cyclic voltammograms of $MoS_{0.5}Se_{1.5}$/C sheets for the initial three cycles scanned between 0.001 and 3.0 V at a rate of 0.1 mV s^{-1}; (b) Discharge-charge curves of the initial three cycles of $MoS_{0.5}Se_{1.5}$/C sheets; (c) Cycling performances of $MoS_{0.5}Se_{1.5}$/C sheets and $MoSe_2$/C sheets at 100 mA g^{-1}; (d) Rate capability of $MoS_{0.5}Se_{1.5}$/C sheets and $MoSe_2$/C sheets at different current densities.

The table of contents entry

A promising anode has been developed for Li-ion batteries consisting of novel $MoS_{0.5}Se_{1.5}$ particles embedded in porous carbon sheets via a facile and cost-effective KCl-assisted strategy. The improved electronic conductivity of $MoS_{0.5}Se_{1.5}$ provides fast transport of both ions and electrons within the electrode; while the volume expansion and aggregation of $MoS_{0.5}Se_{1.5}$ can be avoided due to the intimate contact between $MoS_{0.5}Se_{1.5}$ and porous carbon sheets.

TOC Keyword: battery

Authors: Tongfei Li, Ao Wang, Xin Li, Jingchun Wang, Jie Zhang, Gengtao Fu,* Lin Xu, Dongmei Sun and Yawen Tang*

Title: $MoS_{0.5}Se_{1.5}$ Embedded in Two-dimensionally Porous Carbon Sheets Boost Lithium Storage Performance as An Anode Material

TOC Figure